

RESEARCH

Open Access



Robust adaptive beamforming based on covariance matrix reconstruction using Gauss–Legendre quadrature and steering vector estimation

Yan Lv, Fei Cao , Fan Wu, Chuan He and Xiaowei Feng

*Correspondence:
caofei101@126.com

Rocket Force University
of Engineering, Xi'an 710025,
China

Abstract

The performance of adaptive beamforming is considerably affected by system errors in the gain and phase perturbation errors, direction of arrival mismatch, and incoherent local scattering, especially when the sample data contains the signal of interest (SOI) component. In this study, a robust adaptive beamforming approach based on interference plus noise covariance matrix (INCM) reconstruction using Gauss–Legendre quadrature (GLQ) and steering vector (SV) estimation is developed. The proposed algorithm incorporates the GLQ with the integral over the spherical uncertainty set and uses a linear combination of the integral at several angular nodes to substitute the integral of the entire interference region; consequently, the computational efficiency of reconstructing the INCM is enhanced. The SV of the SOI is represented as a linear combination of several principal eigenvectors of the SOI covariance matrix; thus, the double-constrained problem corresponding to the noise subspace is transformed into a single-constrained model, and its solution can be gained by utilizing the Lagrange multiplier method. Subsequently, the weight vector of the proposed beamformer can be calculated. Numerical simulations indicate that the proposed approach can effectively suppress interferences and exhibits superior overall performance under system errors.

Keywords: Robust adaptive beamforming, Covariance matrix reconstruction, Gauss–Legendre quadrature, SV estimation

1 Introduction

In sensor arrays, which are also regarded as smart antennas, the antenna system can be controlled by a computer, thus substantially improving the performance of the antenna system. Smart antennas have advantages such as high spatial resolution, increased signal to interference plus noise ratio (SINR), and the capability of spatial interference suppression [1]. Adaptive beamforming, a fundamental technology used in sensor arrays, is applicable to a wide range of fields, for example, radar, wireless communication, astronomy, and electronic surveillance [2–5]. This technology can orient the mainlobe toward

the signal of interest (SOI) while forming nulls in the directions of arrival (DOA) of the interferences based on the remaining degrees of freedom of the sensor array. However, in practical applications, there are inevitable mismatches in the signals received by the sensor array, such as gain and phase perturbation errors, DOA mismatch, and incoherent local scattering [6]. These errors severely degrade the performance of the beamformers, especially when the SOI component is present in the received data [7].

Therefore, numerous robust adaptive beamforming (RAB) techniques are developed to enhance output performance even in error scenarios. Examples include diagonal loading techniques, eigen-subspace methods, and worst-case-based approaches [8–11]. These methods are efficient for mild gain and phase perturbation errors and DOA mismatch, but they are ineffective in case of severe system errors. Further, the weight vectors calculated using these methods are based on the sample covariance matrix (SCM). It considerably differs from the theoretical interference plus noise covariance matrix (INCM) when the received number of snapshots is finite [12]. In addition, the existence of the SOI limits the performance of the beamformer under the condition of high-level signal to noise ratio (SNR).

To moderate the impact of SOI component, a number of approaches on the basis of INCM reconstruction using the principle of standard Capon beamformer (SCB) have been developed; consequently, an excellent output SINR has been achieved even in scenarios with a high input SNR [13]. These algorithms can be mainly divided into four types. In the first type, the INCM is reconstructed by uniformly sampling the angular sectors associated with the interference signals [14, 15]. The INCM reconstruction method on the basis of the Capon spectrum integral was first proposed in [14], and the reconstructed INCM was then utilized for formulating a quadratic optimization model to modify the steering vector (SV) of SOI. This algorithm performs well at high SNR, but its performance is limited when the DOA mismatches of incident signals are severe. In [15], the SV of SOI and the eigenvectors of SCM were considered to have a relatively intense correlation, such that the eigenvector of the maximum correlation coefficient was selected as the estimated SV. This approach effectively reduces the computational complexity of SV estimation; however, the correlation between them is inevitably affected when the DOA mismatches are large. To further reduce the complexity of INCM reconstruction, a novel beamformer was devised employing spatial power spectrum sampling [16]. The method is of excellent computational efficiency. Nevertheless, its output SINR will degrade along with the decreasing number of sensors. In [17], the Gauss–Legendre quadrature (GLQ) was introduced for INCM reconstruction using a linear combination of the covariance matrices at three nodes, and the algorithm exhibited reduced computational complexity. The maximum entropy power spectrum principle was used to estimate the powers of incident signals in [18]; consequently, the number of sampling points involved in INCM reconstruction was effectively reduced. However, the usage of linear integral restricts the collection of more potential information, which is an imperfection of the aforementioned algorithms.

The second type is based on the first one by reformulating the interference region, which is constrained by uncertainty sets. The integral over uncertainty sets can be utilized to obtain potential information [19–21]. In [19], an INCM reconstruction method based on the integral of annular uncertainty sets was proposed. It employs multitudes

of discrete uncertainty sets to constrain the angular sectors where the interferences are located and computes the volume integral over these uncertainty sets. The approach stated in [19] outperforms the method in [14] but significantly increases the computational complexity. The INCM reconstruction method proposed in [20] was analogous to the approach of [19]. Based on the intersection of two signal subspaces corresponding to the SCM and SOI covariance matrix, the SV of the desired signal was then obtained. The simulated and experimental results revealed that the algorithm is able to align the main-lobe to the desired signal while effectively suppressing the interferences and possesses better robustness to multiple system errors. In [21], the k -means clustering method was employed to preprocess the sampling points which are located on the surface of the uncertainty set and a few representative sampling points instead of the integral over the entire surface were selected, thus effectively reducing the number of sampling points within the uncertainty set. Through simulation results under one kind of system error, it was verified that the selection of representative sampling points can be accomplished by one iteration. The feasibility of this approach under several other typical system errors remains to be verified.

The third type reconstructs the INCM in the theoretical form by optimizing the SV and estimating the powers of incident signals [22, 23]. In [22], a procedure analogous to the approaches in [9, 14] was employed to estimate the SVs of interferences. Then, the interference powers were derived according to the assumption of orthogonality between distinct SVs of incident signals. Subsequently, the INCM could be reconstructed following its theoretical form. However, the accuracy of SV estimation for the interference signals depends on an ad hoc parameter. The algorithm in [23] compensated for the angle-related bases in the INCM reconstruction by employing the subspace orthogonality technique and subspace fitting method to mitigate undesirable effects of system errors. Another approach for reconstructing INCM by subtracting the reconstructed SOI covariance matrix from the SCM was proposed in [24, 25]. However, these methods almost perform unsatisfactorily when the number of snapshots is low. The last type reconstructs the INCM by projecting the SCM into the interference subspace [26, 27]. In [26], a positive definite matrix was yielded by the integral of angular sectors associated with the interference region, and eigenvectors corresponding to several larger eigenvalues were selected to construct the interference subspace; the SCM was projected into this subspace to eliminate the SOI component. Based on [26], the computational complexity of [27] decreased in the process of computing the positive definite matrix within the interference region, which was obtained by using a fourth-order GLQ. However, the performance of this algorithm is inadequate if there are large DOA errors as well as gain and phase perturbation errors.

Motivated by the works in [17, 19], a novel RAB method based on both INCM reconstruction using the GLQ and SV estimation is developed in this study. The proposed algorithm aims to collect more potential information of the incident signals with reduced computational complexity and to obtain the precise SV of the SOI. The contributions are as given below:

1. We combine the GLQ with the integral over spherical uncertainty set and apply a linear combination of the integral at several angular nodes to reconstruct the INCM with reduced computational complexity.
2. Based on several principal eigenvectors of the SOI covariance matrix, the double-constrained problem is transformed into a single-constrained model, and the SV of the SOI is derived through the Lagrange multiplier method.
3. The steps and computational complexity of the proposed approach are discussed, and numerical simulations are conducted to verify the performance of our proposed algorithm.

The remainder of this paper is as follows. In Sect. 2, the problem background is briefly described. Our proposed algorithm is elaborated in Sect. 3. Section 4 presents numerical simulations and discussion, and the conclusions are summarized in Sect. 5.

2 Problem background

Consider that $L + 1$ incoherent signals impinge on a uniform linear array (ULA) with distinct directions $\{\theta_0, \theta_1, \dots, \theta_L\}$, where the incident sources are from a far-field and narrowband. The ULA is composed of M sensors with the configuration illustrated in Fig. 1. The $M \times 1$ vector received at the instant k is then formulated as [28]

$$\mathbf{x}(k) = \mathbf{x}_s(k) + \mathbf{x}_i(k) + \mathbf{n}(k), \quad (1)$$

where $\mathbf{x}_s(k) = \mathbf{a}(\theta_0)s_0(k)$ and $\mathbf{x}_i(k) = \sum_{l=1}^L \mathbf{a}(\theta_l)s_l(k)$ are the SOI and interference components, respectively, $\mathbf{n}(k)$ stands for the Gaussian noise with variance σ_n^2 , $s_l(k)$ denotes the signal waveform, and $\mathbf{a}(\theta_l)$, abbreviated as \mathbf{a}_l , are the SVs of incident signals, which are given as

$$\mathbf{a}_l = [1, e^{j2\pi d \sin \theta_l / \lambda}, \dots, e^{j2\pi(M-1)d \sin \theta_l / \lambda}]^T, \quad l = 0, 1, \dots, L \quad (2)$$

Here, $(\bullet)^T$ denotes the transpose operator, $d = \lambda/2$ and λ represent the inter-element spacing and the wavelength of $s_l(k)$, respectively.

For the weight vector $\mathbf{w} = [w_1, w_2, \dots, w_M]^T$, the output SINR is defined as

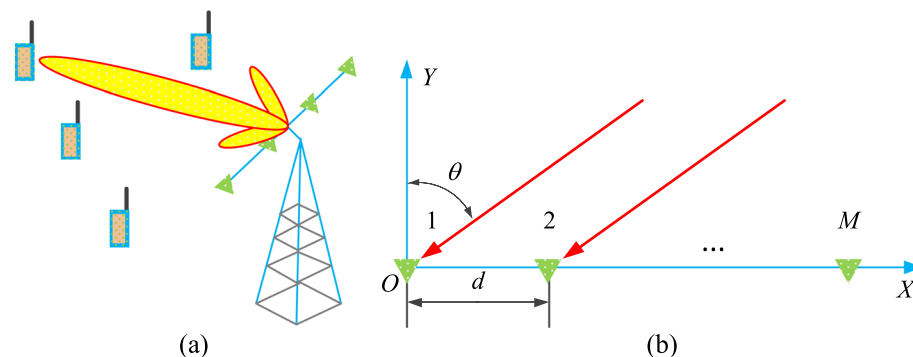


Fig. 1 Signal model. **a** Classical application of adaptive beamforming in wireless communication, with the mainlobe pointing toward the user. **b** ULA configuration

$$\text{SINR} = \frac{\sigma_0^2 |\mathbf{w}^H \mathbf{a}_0|^2}{\mathbf{w}^H \mathbf{R}_{i+n} \mathbf{w}}, \quad (3)$$

where $\sigma_0^2 = E\{s_0(k)s_0^H(k)\}$ is the SOI power, $E(\bullet)$ stands for the expectation operator, and $(\bullet)^H$ denotes the Hermitian transpose. Correspondingly, \mathbf{R}_{i+n} is the $M \times M$ dimensional theoretical INCM, indicated by

$$\mathbf{R}_{i+n} = \mathbf{R}_i + E\{\mathbf{n}(k)\mathbf{n}^H(k)\} = \sum_{l=1}^L \sigma_l^2 \mathbf{a}_l \mathbf{a}_l^H + \sigma_n^2 \mathbf{I}, \quad (4)$$

where σ_l^2 represents the l th interference power and \mathbf{I} denotes M -order identity matrix. The SCB aims at suppressing interference components while maintaining the SOI without any distortion, leading to maximized output SINR. The SCB is formulated as

$$\mathbf{w} = \arg \min_{\mathbf{w}} \mathbf{w}^H \mathbf{R}_{i+n} \mathbf{w}, \quad \text{s.t. } \mathbf{w}^H \mathbf{a}_0 = 1, \quad (5)$$

whose solution has the following general form:

$$\mathbf{w}_{SCB} = \frac{\mathbf{R}_{i+n}^{-1} \mathbf{a}_0}{\mathbf{a}_0^H \mathbf{R}_{i+n}^{-1} \mathbf{a}_0}. \quad (6)$$

The optimal SINR can be calculated as

$$\text{SINR}_{\text{opt}} = \sigma_0^2 \mathbf{a}_0^H \mathbf{R}_{i+n}^{-1} \mathbf{a}_0. \quad (7)$$

Accordingly, the beam pattern of SCB can be derived as

$$\text{Beam}(\theta) = 20 \times \lg \left\{ \frac{|\mathbf{w}_{SCB}^H \mathbf{a}(\theta)|}{\max |\mathbf{w}_{SCB}^H \mathbf{a}(\theta)|} \right\}, \quad (8)$$

where θ is the angle in the scanning interval, $\mathbf{a}(\theta)$ can be obtained by using the prior knowledge of array configuration, and $\lg(\bullet)$ represents the logarithmic operator with base 10. In practical applications, the exact \mathbf{a}_0 and \mathbf{R}_{i+n} are typically infeasible and are normally replaced by the nominal SV $\mathbf{a}(\hat{\theta}_0)$ (abbreviated as $\hat{\mathbf{a}}_0$) and SCM, given by

$$\hat{\mathbf{R}}_x = \frac{1}{K} \sum_{k=1}^K \mathbf{x}(k) \mathbf{x}^H(k). \quad (9)$$

Here, K denotes the number of snapshots. When K is inadequate or the DOAs of incident signals are mismatched, a large gap is bound to exist between \mathbf{R}_{i+n} and $\hat{\mathbf{R}}_x$.

To reduce the gap with the theoretical INCM and enhance the robustness, a method for reconstructing the INCM is developed [14]:

$$\bar{\mathbf{R}}_{i+n} = \int_{\Theta_{i+n}} \frac{\mathbf{a}(\theta) \mathbf{a}^H(\theta)}{\mathbf{a}^H(\theta) \hat{\mathbf{R}}_x^{-1} \mathbf{a}(\theta)} d\theta, \quad \theta \in \Theta_{i+n}. \quad (10)$$

Here, Θ_{i+n} denotes the entire spatial domain except for the SOI region. Another novel INCM reconstruction method based on the volume integral is employed in [19], which is formulated as follows:

$$\widehat{\mathbf{R}}_{i+n} = \frac{1}{2} \int_{\Theta_i} \mathbf{r}(\theta) d\theta + \hat{\sigma}_n^2 \mathbf{I}, \quad \theta \in \Theta_i, \quad (11)$$

where Θ_i stands for the interference region, and $\hat{\sigma}_n^2$, setting as the minimum eigenvalue of the matrix $\widehat{\mathbf{R}}_x$ [19, 22], represents the estimated noise power. The expression for $\mathbf{r}(\theta)$ is

$$\mathbf{r}(\theta) = \int_{\delta_{\mathbf{a}}(\theta)} \frac{\bar{\mathbf{a}} \bar{\mathbf{a}}^H}{\bar{\mathbf{a}}^H \widehat{\mathbf{R}}_x^{-1} \bar{\mathbf{a}}} d\delta. \quad (12)$$

Here, $\delta_{\mathbf{a}}(\theta) = \{\bar{\mathbf{a}} | \|\bar{\mathbf{a}} - \mathbf{a}(\theta)\|_2 \leq \varepsilon\}$ is the spherical uncertainty set, $\|\bullet\|_2$ represents the Euclidean norm, and ε stands for the threshold of $\delta_{\mathbf{a}}(\theta)$. Equation (11) is usually approximated by the discrete summation of uniform sampling in the intervals $\Theta_l, l = 1, 2, \dots, L$, where the interferences are located. This process can be regarded as the interpolation summation in these intervals, expressed as [19]

$$\widehat{\mathbf{R}}_{i+n} \approx \frac{1}{2} \sum_{l=1}^L \sum_{c=1}^C \mathbf{r}(\theta_{lc}) + \hat{\sigma}_n^2 \mathbf{I}. \quad (13)$$

Here, L and C denote the number of interference signals and sampling points in Θ_l , respectively. Evidently, the computational complexity of Eq. (13) is of sufficient magnitude when the number of sampling points, C , is set high enough to ensure precise INCM reconstruction.

3 Proposed algorithm

3.1 INCM reconstruction

Similar to the assumptions implemented in [20–29], we also assume that the SOI region and the location of interferences are mutually separate. In this subsection, we utilize the GLQ to compute Eq. (13) efficiently, which can be expressed in the following form [17]:

$$\int_{-1}^1 \rho(z) f(z) dz \approx \sum_{j=1}^J A_j f(z_j), \quad (14)$$

where $\rho(z)$ represents the weight function, which is equal to the constant 1 in GLQ; $f(z)$ is the integral function; A_j and $z_j, j = 1, 2, \dots, J$ are independent of $f(z)$ and denote the coefficients and nodes of GLQ, respectively. The nodes are generally the roots of the Legendre polynomial, indicated by

$$\text{Leg}_n(z) = \frac{1}{2^n n!} \frac{d^n}{dz^n} \{(z^2 - 1)^n\}, \quad (15)$$

where n is the order of the Legendre polynomial. Taking the trade-off between computational efficiency and numerical accuracy into account, we implement INCM reconstruction in terms of the fifth-order Legendre polynomial, which can be written as

$$\text{Leg}_5(z) = \frac{1}{8}(63z^5 - 70z^3 + 15z). \quad (16)$$

Five nodes can be obtained according to the roots of Eq. (16):

$$\{z_1, z_2, z_3, z_4, z_5\} = \left\{ -\sqrt{\frac{35 + 2\sqrt{70}}{63}}, -\sqrt{\frac{35 - 2\sqrt{70}}{63}}, 0, \sqrt{\frac{35 - 2\sqrt{70}}{63}}, \sqrt{\frac{35 + 2\sqrt{70}}{63}} \right\}. \quad (17)$$

The following formula can be yielded by substituting Eq. (17) into Eq. (14):

$$\int_{-1}^1 f(z) dz \approx \sum_{j=1}^5 A_j f(z_j). \quad (18)$$

According to the principle of GLQ, Eq. (19) holds true strictly when $f(z)$ is taken in turn with $1, z^1, z^2, z^3$, and z^4 , which yields

$$\begin{aligned} \int_{-1}^1 1 dz &= z_1^0 A_1 + z_2^0 A_2 + z_3^0 A_3 + z_4^0 A_4 + z_5^0 A_5 \\ \int_{-1}^1 z^1 dz &= z_1^1 A_1 + z_2^1 A_2 + z_3^1 A_3 + z_4^1 A_4 + z_5^1 A_5 \\ \int_{-1}^1 z^2 dz &= z_1^2 A_1 + z_2^2 A_2 + z_3^2 A_3 + z_4^2 A_4 + z_5^2 A_5 \\ \int_{-1}^1 z^3 dz &= z_1^3 A_1 + z_2^3 A_2 + z_3^3 A_3 + z_4^3 A_4 + z_5^3 A_5 \\ \int_{-1}^1 z^4 dz &= z_1^4 A_1 + z_2^4 A_2 + z_3^4 A_3 + z_4^4 A_4 + z_5^4 A_5. \end{aligned} \quad (19)$$

Equation (19) can be expressed in another form, $\mathbf{Z}\mathbf{A} = \mathbf{F}$, where $\mathbf{A} = [A_1, A_2, A_3, A_4, A_5]^T$ represents the coefficient vector to be determined, $\mathbf{F} = [2, 0, 2/3, 0, 2/5]^T$, and \mathbf{Z} denotes the node matrix.

$$\mathbf{Z} = \begin{bmatrix} 1 & 1 & 1 & 1 & 1 \\ z_1^1 & z_2^1 & z_3^1 & z_4^1 & z_5^1 \\ z_1^2 & z_2^2 & z_3^2 & z_4^2 & z_5^2 \\ z_1^3 & z_2^3 & z_3^3 & z_4^3 & z_5^3 \\ z_1^4 & z_2^4 & z_3^4 & z_4^4 & z_5^4 \end{bmatrix}. \quad (20)$$

According to Eq. (20), \mathbf{Z} is a 5×5 dimensional Vandermonde matrix. Because the elements of the nodes, $\{z_1, z_2, \dots, z_5\}$, are not equal, \mathbf{Z} is invertible. Therefore, the coefficient vector can be determined as $\mathbf{A} = \mathbf{Z}^{-1}\mathbf{F}$. The variables on the right side of Eq. (18) can then be obtained, and the fifth-order GLQ can be realized.

Since $\{z_1, z_2, \dots, z_5\}$ belong to the interval $[-1, 1]$, the interval used in INCM reconstruction should be $\Theta_l = [\theta_l^{\text{low}}, \theta_l^{\text{up}}]$, $l = 1, 2, \dots, L$; hence, it is unsatisfactory to

reconstruct the INCM using these nodes. We can then linearly map the nodes in the interval $[-1, 1]$ to the angular sectors of L interferences Θ_l as follows [27]:

$$\theta_{lj} = \frac{\theta_l^{up} - \theta_l^{low}}{2} z_j + \frac{\theta_l^{up} + \theta_l^{low}}{2}, \quad j = 1, 2, \dots, 5, \tag{21}$$

where θ_{lj} represent the angular nodes within each interference region bounded by $[\theta_l^{low}, \theta_l^{up}]$. Then, by adjusting the integral interval, Eq. (18) is transformed into

$$\int_{\theta_l^{low}}^{\theta_l^{up}} f(\theta) d\theta \approx \frac{\theta_l^{up} - \theta_l^{low}}{2} \sum_{j=1}^5 A_{lj} f(\theta_{lj}). \tag{22}$$

In Eq. (22), the uninterrupted integral in the interval Θ_l is replaced with a linear combination of the function values of five nodes. Substituting $\mathbf{r}(\theta)$ as the integral function into Eq. (22), the novel INCM can be obtained as follows:

$$\begin{aligned} \tilde{\mathbf{r}}_{i+n} &= \frac{1}{2} \int_{\Theta_i} \mathbf{r}(\theta) d\theta + \hat{\sigma}_n^2 \mathbf{I} = \frac{1}{2} \sum_{l=1}^L \int_{\theta_l^{low}}^{\theta_l^{up}} \mathbf{r}(\theta) d\theta + \hat{\sigma}_n^2 \mathbf{I} \\ &\approx \frac{1}{2} \sum_{l=1}^L \frac{\theta_l^{up} - \theta_l^{low}}{2} \sum_{j=1}^J A_{lj} \mathbf{r}(\theta_{lj}) + \hat{\sigma}_n^2 \mathbf{I} = \frac{\theta_l^{up} - \theta_l^{low}}{4} \sum_{l=1}^L \sum_{j=1}^J A_{lj} \mathbf{r}(\theta_{lj}) + \hat{\sigma}_n^2 \mathbf{I}, \end{aligned} \tag{23}$$

where $J = 5$ and $\mathbf{r}(\theta_{lj})$ is numerically computed as

$$\mathbf{r}(\theta_{lj}) = \sum_{q=1}^Q \frac{\bar{\mathbf{a}}_q \bar{\mathbf{a}}_q^H}{\bar{\mathbf{a}}_q^H \hat{\mathbf{R}}_x^{-1} \bar{\mathbf{a}}_q}. \tag{24}$$

Here, Q denotes the number of sampling points within the uncertainty set, and $\bar{\mathbf{a}}_q \in \delta_{\mathbf{a}}(\theta_{lj})$ stands for the SVs located at the surface of the sphere around $\mathbf{a}(\theta_{lj})$ because $\delta_{\mathbf{a}}(\theta_{lj})$ contains collinear SVs [19]. For the sake of clarity, the comparison between Eqs. (13) and (23) is shown schematically in Fig. 2. The essence of Eq. (23) is to replace

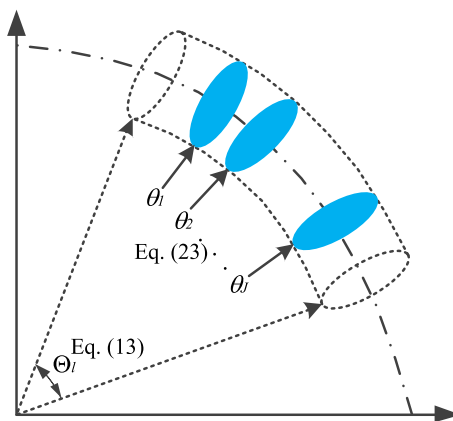


Fig. 2 Concept of INCM reconstruction method based on GLQ and uncertainty sets

the volume integral in the dashed region with a linear combination of the integral over J spherical uncertainty sets colored in blue. Additionally, the number of sampling points in Eq. (23) within each interference interval is significantly fewer than that in Eq. (13) owing to the use of GLQ. Therefore, the proposed GLQ-based operational method can enhance the computational efficiency of the algorithm stated in [19]. Furthermore, the performance of the reconstructed $\tilde{\mathbf{R}}_{i+n}$ is evaluated through numerical simulations explained in Sect. 4.1.

3.2 SV correction of the SOI

The eigen-decomposition of SCM is as follows:

$$\hat{\mathbf{R}}_x = \sum_{m=1}^M \alpha_m \mathbf{u}_m \mathbf{u}_m^H = \mathbf{U}_s \mathbf{\Lambda}_s \mathbf{U}_s^H + \mathbf{U}_n \mathbf{\Lambda}_n \mathbf{U}_n^H. \quad (25)$$

Here, $\alpha_M \leq \dots \leq \alpha_1$ stand for eigenvalues of $\hat{\mathbf{R}}_x$, \mathbf{u}_m represents the eigenvectors of α_m , $\mathbf{U}_s = [\mathbf{u}_1, \mathbf{u}_2, \dots, \mathbf{u}_{L+1}]$ spans the signal subspace, and $\mathbf{U}_n = [\mathbf{u}_{L+2}, \dots, \mathbf{u}_M]$ represents the noise subspace. Because the number of sources, $L + 1$, can be got by applying the approach developed in [30], it is assumed that the number of sources is known as prior information [31]. On the basis of the orthogonality associated with the signal and noise subspaces, because the actual SV, \mathbf{a}_0 , belongs to the former, the following formula can be derived:

$$\mathbf{a}_0^H \mathbf{U}_n \mathbf{U}_n^H \mathbf{a}_0 = 0. \quad (26)$$

Thereafter, according to Eq. (26), the SV estimation problem can be described as [16]

$$\begin{aligned} \min_{\tilde{\mathbf{a}}_0} & \tilde{\mathbf{a}}_0^H \mathbf{U}_n \mathbf{U}_n^H \tilde{\mathbf{a}}_0 \\ \text{s.t.} & \|\tilde{\mathbf{a}}_0 - \hat{\mathbf{a}}_0\|_2 \leq \varepsilon \\ & \|\tilde{\mathbf{a}}_0\|_2 = \sqrt{M}, \end{aligned} \quad (27)$$

where $\tilde{\mathbf{a}}_0$ denotes the optimized SV. The first constraint of Eq. (27) represents an uncertainty set restriction on $\tilde{\mathbf{a}}_0$, which guarantees that the optimal value is searched in the neighborhood of $\hat{\mathbf{a}}_0$ and prevents its convergence to the interference SV. The second constraint restricts the constant modulus to $\tilde{\mathbf{a}}_0$.

Similarly, the SOI covariance matrix, $\tilde{\mathbf{R}}_s$, can be obtained from Eq. (23), and its eigen-decomposition yields

$$\tilde{\mathbf{R}}_s = \frac{\theta_0^{\text{up}} - \theta_0^{\text{low}}}{4} \sum_{j=1}^J A_j \mathbf{r}(\theta_{0j}) + \hat{\sigma}_n^2 \mathbf{I} = \sum_{m=1}^M \tau_m \mathbf{v}_m \mathbf{v}_m^H. \quad (28)$$

A column orthogonal matrix $\mathbf{V}_\eta = [\mathbf{v}_1, \mathbf{v}_2, \dots, \mathbf{v}_\eta]$ composed of several principal eigenvectors can then be formed. The η eigenvalues occupy most of the energy of all eigenvalues; thus, $\tilde{\mathbf{R}}_s \approx \mathbf{V}_\eta \mathbf{\Xi} \mathbf{V}_\eta^H$ can be obtained, where the diagonal elements of $\mathbf{\Xi}$ are filled with η largest eigenvalues of $\tilde{\mathbf{R}}_s$. Hence, \mathbf{V}_η spans the signal subspace, which suggests that the SV of the SOI can be formulated as a linear combination corresponding to the columns of \mathbf{V}_η [32]. Consequently, the SV of SOI is expressed as

$$\tilde{\mathbf{a}}_0 = \sqrt{M} \mathbf{V}_\eta \mathbf{b}, \quad (29)$$

where \mathbf{b} is the rotating vector with $\|\mathbf{b}\|_2 = 1$. $\tilde{\mathbf{R}}_s$ originates from the volume integral of $\hat{\mathbf{a}}_0$, and the SV located at the spherical uncertainty set can be expressed on the basis of \mathbf{V}_η ; therefore, $\tilde{\mathbf{a}}_0 \in \delta_a(\hat{\theta}_0)$ can be obtained, i.e., $\|\tilde{\mathbf{a}}_0 - \hat{\mathbf{a}}_0\|_2 \leq \varepsilon$ always holds true. Thus, Eq. (29) ensures that the optimal SV is searched in the neighborhood of $\hat{\mathbf{a}}_0$, and there is no possibility of convergence to the interference SV. Subsequently, the first constraint in Eq. (27) can be omitted. Substituting Eq. (29) into Eq. (27), the following formula can be derived:

$$\begin{aligned} \min_{\mathbf{b}} M \mathbf{b}^H \mathbf{R}_V \mathbf{b} \\ \text{s.t. } \|\mathbf{b}\|_2 = 1, \end{aligned} \quad (30)$$

where $\mathbf{R}_V = \mathbf{V}_\eta^H \mathbf{U}_n \mathbf{U}_n^H \mathbf{V}_\eta$. In Eq. (30), M is a constant term and can be omitted.

$$\begin{aligned} \min_{\mathbf{b}} \mathbf{b}^H \mathbf{R}_V \mathbf{b} \\ \text{s.t. } \|\mathbf{b}\|_2 = 1. \end{aligned} \quad (31)$$

On the basis of the Lagrange multiplier method [33], we derive the solution for Eq. (31). The Lagrangian function is constructed as

$$L(\mathbf{R}_V, \mathbf{b}) = \frac{1}{2} \mathbf{b}^H \mathbf{R}_V \mathbf{b} + \xi (1 - \mathbf{b}^H \mathbf{b}), \quad (32)$$

where ξ represents the Lagrange multiplier. Thereafter, we calculate the derivative of Eq. (32) and solve for its root as follows:

$$\frac{\partial L(\mathbf{R}_V, \mathbf{b})}{\partial \mathbf{b}} = \mathbf{R}_V \mathbf{b} - \xi \mathbf{b} = 0. \quad (33)$$

According to Eq. (33), we obtain $\mathbf{R}_V \mathbf{b} = \xi \mathbf{b}$. Substituting Eq. (33) into Eq. (31), we can conclude that to minimize the objective function, ξ should be the minimum eigenvalue of \mathbf{R}_V and \mathbf{b} is the eigenvector corresponding to this minimum eigenvalue, denoted as \mathbf{b}_η . Therefore, $\tilde{\mathbf{a}}_0 = \sqrt{M} \mathbf{V}_\eta \mathbf{b}_\eta$ can be gained.

The weight vector of the array can be yielded with the resulting $\tilde{\mathbf{R}}_{i+n}$ and $\tilde{\mathbf{a}}_0$:

$$\mathbf{w} = \frac{\tilde{\mathbf{R}}_{i+n}^{-1} \tilde{\mathbf{a}}_0}{\tilde{\mathbf{a}}_0^H \tilde{\mathbf{R}}_{i+n}^{-1} \tilde{\mathbf{a}}_0}. \quad (34)$$

3.3 Summary of the proposed algorithm

Unlike previous methods, the proposed approach incorporates the GLQ with the integral of spherical uncertainty sets to obtain more comprehensive information while reducing computational complexity. The idea of our work is partly inspired by [19]. However, the computational complexity of the algorithm in [19] is high, which is reduced in our study by introducing GLQ. It can be considered as an improved version combining the advantage of [17, 19]. Consequently, the INCM and SOI covariance matrix can be reconstructed more accurately compared with traditional

methods. In addition, the nominal SV of SOI can be corrected adequately through the foregoing SV estimate operation. A summary of the proposed algorithm is listed below:

Steps	Details
(1)	Compute the coefficients A_j and nodes z_j of GLQ by applying Eqs. (16) and (19)
(2)	Calculate the angular nodes using Eq. (21), and reconstruct $\tilde{\mathbf{R}}_{i+n}$ through Eq. (23)
(3)	Obtain the optimized $\tilde{\mathbf{a}}_0$ via Eqs. (28) and (29), and derive the weight vector using Eq. (34)

According to the steps of our method, Step (1) can be derived in advance according to the order of GLQ; hence, the complexity of our algorithm is mainly concentrated in Steps (2) and (3) and is roughly $O\{\max(JQM^2, M^3)\}$. As J is significantly less than C , it is apparent that our approach is preferable to the algorithm stated in [19] ($O\{\max(CQM^2, M^{3.5})\}$) in terms of computational complexity.

4 Results and discussion

In this part, consider three incident signals impinging on the ULA of 10 sensors from $\theta_0 = 0^\circ$, $\theta_1 = -50^\circ$, and $\theta_2 = 40^\circ$, where the first signal is treated as the SOI component, and its power is set to SNR = 20 dB, when the SINR is compared with number of snapshots. To compare the SINR with SNR, $K = 30$ is fixed. The remaining signals are viewed as interferences with a power of 30 dB. The integral interval is set within $\pm 8^\circ$ [19, 26, 31] of the nominal DOAs $\hat{\theta}_l$, $l = 0, 1, 2$, which are regarded as the prior information [19, 20]; therefore, the integral intervals of the SOI and interferences are $\Theta_0 = [\theta_0^{\text{low}}, \theta_0^{\text{up}}] = [\hat{\theta}_0 - 8^\circ, \hat{\theta}_0 + 8^\circ]$ and $\Theta_l = [\theta_l^{\text{low}}, \theta_l^{\text{up}}] = [\hat{\theta}_l - 8^\circ, \hat{\theta}_l + 8^\circ]$, $l = 1, 2$, respectively. In all simulations, the results are obtained from 200 Monte Carlo simulation runs [20–33].

The proposed approach is compared with the spatial matched filter (SMF) method that is user parameter-free [8]; the fixed diagonal loading (FDL) algorithm [13]; the reconstruction-based beamformers: INCM-linear [14], INCM-volume [19], and INCM-ISV [22]; as well as the GLQ-based algorithms: GL-linear [17] and GL-subspace [27]. For the FDL algorithm, the diagonal loading level is set to $\sigma_l^2 = 10$ dB. For the GL-subspace approach, $N = 5$ is chosen during the construction of the projection matrix. In the INCM-volume beamformer, $C = 40$ are adopted. In our proposed method, $\eta = 4$ [32] and the model for discrete sampling within $\delta_a(\theta_{lj})$ is consistent with the INCM-volume algorithm:

$$\bar{\mathbf{a}}_q = \mathbf{a}(\theta_{lj}) + \frac{\varepsilon}{\sqrt{M}} [e^{j\phi_0^q}, e^{j\phi_1^q}, \dots, e^{j\phi_{M-1}^q}]^T. \quad (35)$$

Here, $\varepsilon = \sqrt{0.1}$, and ϕ_m^q , $m = 0, 1, \dots, M-1$ is chosen as 0 and π , i.e., $Q = \chi^M = 2^M = 1024$, in which χ denotes the number of sampling points in $[0, 2\pi)$.

4.1 Performance comparison under different orders of GLQ

To evaluate the similarity between $\tilde{\mathbf{R}}_{i+n}$ and $\hat{\mathbf{R}}_{i+n}$, their correlation coefficients for different GLQ orders are first calculated [17, 31], which can be defined as

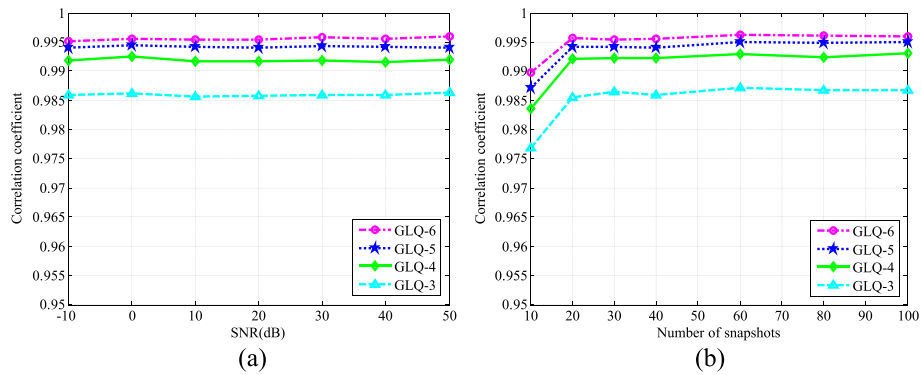


Fig. 3 Comparison of correlation coefficient values. **a** Correlation coefficient for covariance matrix under different GLQ orders against SNR. **b** Correlation coefficient against number of snapshots

Table 1 Comparison of running times for different GLQ orders

Algorithms	INCM-volume	GLQ-6	GLQ-5	GLQ-4	GLQ-3
Times/s	2.1584	0.3340	0.2771	0.2173	0.1624
Complexity	$O\{CQM^2\}$	$O\{JQM^2\}$			

$$\text{cor}(\tilde{\mathbf{R}}_{i+n}, \hat{\mathbf{R}}_{i+n}) = \frac{|\text{vec}(\tilde{\mathbf{R}}_{i+n})^H \text{vec}(\hat{\mathbf{R}}_{i+n})|}{\|\text{vec}(\tilde{\mathbf{R}}_{i+n})\|_2 \|\text{vec}(\hat{\mathbf{R}}_{i+n})\|_2}. \tag{36}$$

Here, $\text{vec}(\bullet)$ is the vectorization operator. In each simulation, the nominal DOAs of incident signals are randomly distributed in the interval $\hat{\theta}_l \in [\theta_l - 8^\circ, \theta_l + 8^\circ]$, $l = 0, 1, 2$. Figure 3a presents the comparison of the correlation coefficient and SNR when the order of GLQ is set to $J = 3, 4, 5$, and 6, where GLQ-3 represents the third-order GLQ. We can conclude that the higher the order of GLQ, the greater the similarity of $\tilde{\mathbf{R}}_{i+n}$ and $\hat{\mathbf{R}}_{i+n}$; in other words, the gap between $\tilde{\mathbf{R}}_{i+n}$ and $\hat{\mathbf{R}}_{i+n}$ decreases gradually. Furthermore, the correlation coefficients for $J = 5$ and $J = 6$ are in the neighborhood of 0.995. The plot of correlation coefficient versus number of snapshots is manifested in Fig. 3b. Once the number of snapshots exceeds 20, the correlation coefficients of GLQ-6 and GLQ-5 tend to level off. Despite the high number of snapshots, GLQ-4 and GLQ-3 still exhibit slight fluctuations in the output curves. The running time taken for each execution is listed in Table 1. A MATLAB 2014a environment with 4G RAM is used. It is evident that dense sampling in the interval Θ_l results in a longer execution time for different GLQ orders.

The output SINR versus SNR for different GLQ orders is illustrated in Fig. 4a, and the deviation from the optimal SINR is depicted in Fig. 4b. The SINRs associated with GLQ-5 and GLQ-6 are slightly lower than the output of INCM-volume algorithm. Since the output SINRs of GLQ-5 and GLQ-6 converge to almost the same level and the GLQ-5 has reduced computational complexity and running time, the fifth-order GLQ is preferred to reconstruct the INCM. The plot of SINR versus number of snapshots is displayed in Fig. 4c, and it is demonstrated that the performance corresponding to GLQ-5

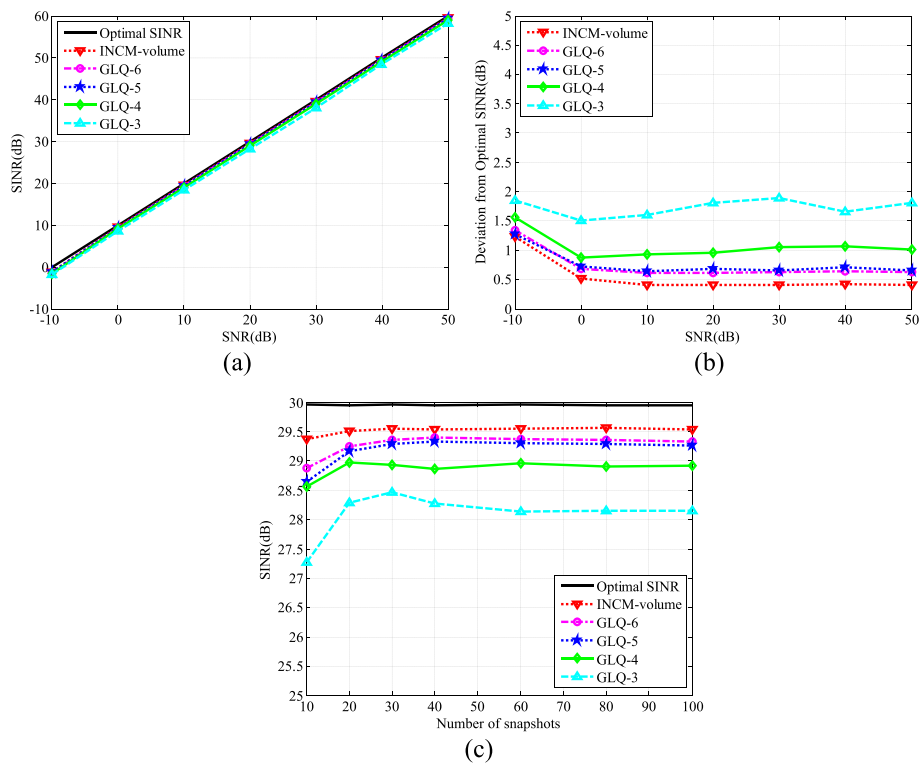


Fig. 4 Comparison of SINR. **a** SINR versus SNR. **b** Deviation against SNR. **c** SINR against number of snapshots

and GLQ-6 is relatively stable with $K \geq 30$. In addition, the output curves of GLQ-3 and GLQ-4 fluctuate as the number of snapshots varies. Thus, the feasibility of applying the GLQ rather than the integral by uniform sampling in the interference region as well as the reasonability of adopting $J = 5$ for balancing the computational efficiency and ensuring the output performance are verified.

4.2 DOA random mismatch

In the second example, the performance of tested beamformers in terms of DOA random error is assessed. The nominal DOAs of all incident signals are the same as those described in Sect. 4.1. Figure 5a, b compares the output SINR versus SNR. It is evident that the output curves associated with the SMF and FDL algorithms deteriorate gradually with increase in SNR owing to the self-cancellation phenomenon generated by the SOI component. In contrast, the performance of our proposed algorithm and INCM-volume method gradually improves as the SNR increases, and they outperform other approaches at different tested SNR values. Figure 5c presents the plot of SINR against number of snapshots. The INCM-volume approach and our proposed method outperform the remaining algorithms associated with the output performance, which approaches the optimal value, and the performance of both remains stable as K exceeds 30. In contrast, the output curves of the SMF and FDL beamformers are incapable of displaying a significant increasing trend as K increases from 10 to 100.

Subsequently, to investigate the output performance with different interference powers, the powers of the two interferences are randomly distributed in [25 dB, 35 dB]

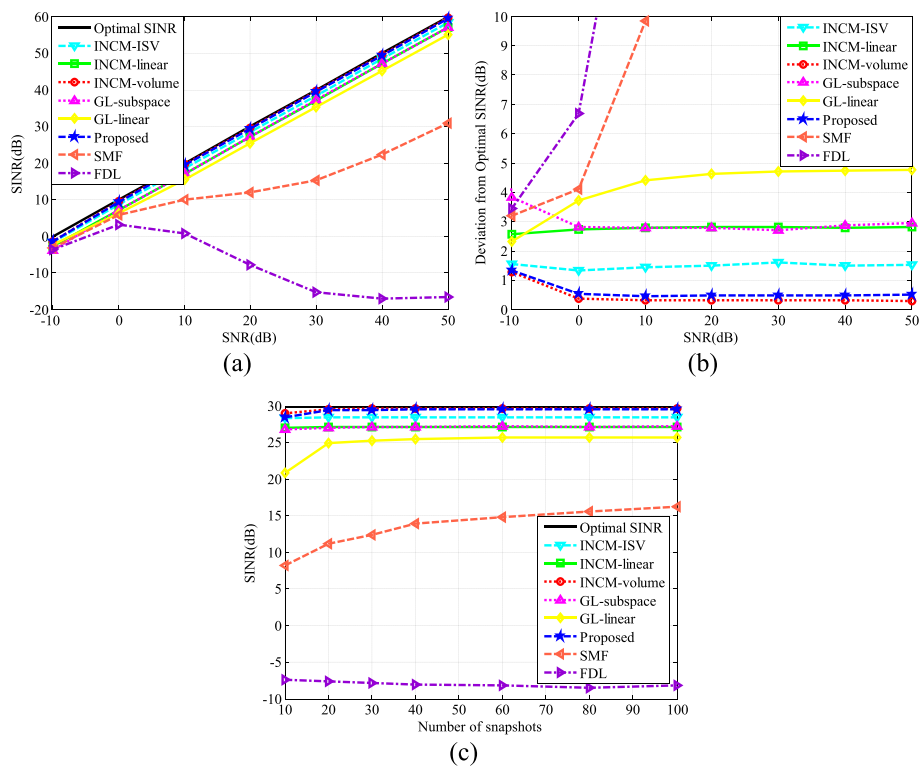


Fig. 5 Performance comparison. **a** SINR versus SNR. **b** Deviation against SNR. **c** SINR against number of snapshots

during each test. Accordingly, the gap between the two interference powers is defined within $[-10 \text{ dB}, 10 \text{ dB}]$. Figure 6a, b reveals the plot of both SINR and the deviation from optimal SINR versus SNR. It is observed that the output curves of the proposed algorithm and INCM-volume method are almost unaffected by random variations of interference powers. The output performance of the INCM-linear and GL-subspace approaches exhibits mild degradations. The plot of SINR versus number of snapshots is showcased in Fig. 6c. Similarly, the performance of our proposed algorithm is marginally lower than that of the INCM-volume method and is superior to the remaining approaches.

4.3 Incoherent local scattering

In the third simulation, the SOI component is considered to possess the property of time-varying [14]:

$$\mathbf{x}_s(k) = \mathbf{a}_0 s_0(k) + \sum_{\beta=1}^4 \mathbf{a}(\theta_\beta) s_\beta(k), \beta = 1, 2, \dots, 4, \tag{37}$$

where θ_β is randomly distributed in $N(\theta_0, 4^\circ)$ in each run, $\mathbf{a}(\theta_\beta)$ is the SV corresponding to θ_β , and $s_\beta(k)$ is followed a Gaussian generator of $N(0, 1)$. In this case, it is impossible for $\text{rank}(\mathbf{R}_s) = 1$, where \mathbf{R}_s and $\text{rank}(\bullet)$, respectively, denote the SOI covariance matrix

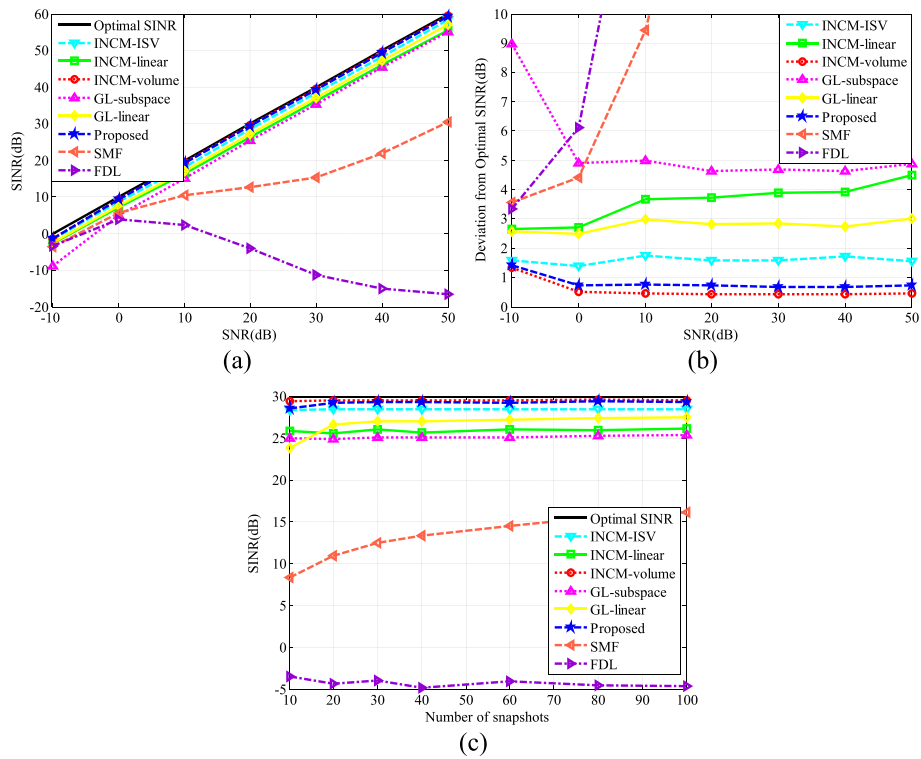


Fig. 6 Results of different interference powers. **a** SINR against SNR. **b** Deviation versus SNR. **c** SINR against number of snapshots

and the rank of \mathbf{R}_s ; therefore, the SINR and weight vector are calculated by the following general forms:

$$\text{SINR} = \mathbf{w}^H \mathbf{R}_s \mathbf{w} / \mathbf{w}^H \mathbf{R}_{i+n} \mathbf{w}, \tag{38}$$

$$\mathbf{w} = \Phi \left\{ \tilde{\mathbf{R}}_{i+n}^{-1} \mathbf{R}_s \right\}, \tag{39}$$

where $\mathbf{R}_s = \frac{1}{K} \sum_{k=1}^K \mathbf{x}_s(k) \mathbf{x}_s^H(k)$, and $\Phi\{\bullet\}$ is the extracted main eigenvector. The output SINR against SNR and the departure from the optimal curve versus SNR are, respectively, depicted in Fig. 7a, b. It is indicated that the performance of our proposed algorithm and GL-linear algorithm is remarkably comparable while the SNR is less than 10 dB. However, as the SNR exceeds 10 dB, the SINR of our method is slightly lower than that of the GL-linear approach and is superior to the remaining algorithms. Figure 7c depicts the plot of SINR against the number of snapshots. Evidently, the output curve of our approach rarely fluctuates with the number of snapshots once it exceeds 30.

4.4 Gain and phase perturbation errors

In the fourth scenario, the effect corresponding to gain and phase perturbation is tested. If this mismatch exists in the signal model, the m th term of (2) becomes [22]

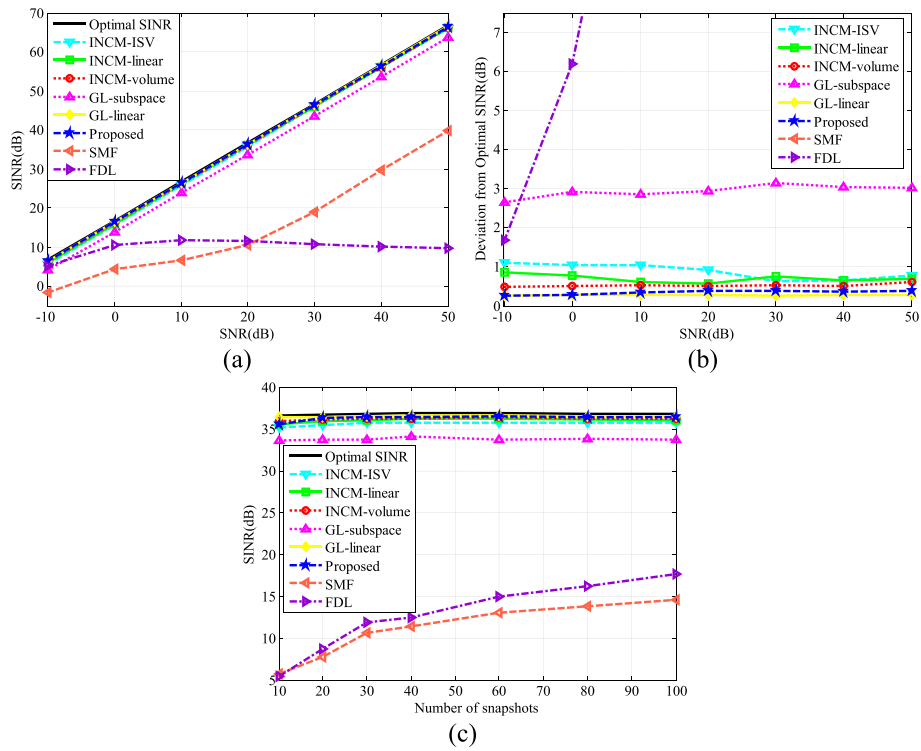


Fig. 7 Performance comparison for the last simulation. **a** SINR against SNR. **b** Deviation versus SNR. **c** SINR against number of snapshots

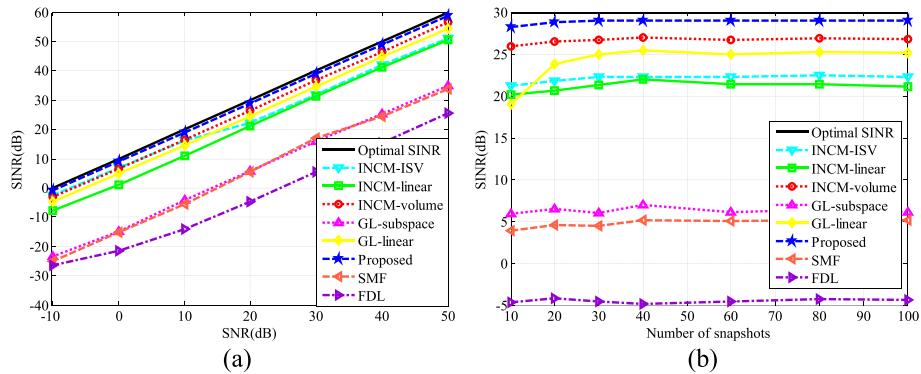


Fig. 8 Comparison of SINR. **a** SINR against SNR. **b** SINR against number of snapshots

$$\mathbf{a}_l^{(m)} = (1 + \kappa_m) e^{j(2\pi \frac{md \sin \theta_l}{\lambda} + \tau_m)}. \quad (40)$$

Here, κ_m and τ_m are the gain and phase perturbation errors at m th element obeyed the Gaussian distributions $N(1, 0.1)$ and $N(0, 0.2\pi)$, respectively. The plot of SINR versus SNR is presented in Fig. 8a. It is undoubted that our proposed algorithm behaves the best among all the rivals. In contrast, the SMF and GL-subspace algorithms exhibit significant degradation in performance, and they display analogous trends in their output curves. The performance of the investigated participants versus number of snapshots is illustrated in Fig. 8b. Apparently, our proposed approach is almost independent of the

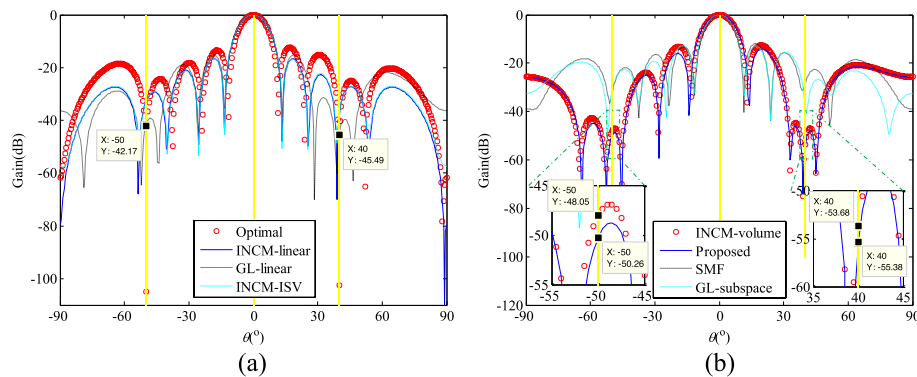


Fig. 9 Beam patterns for investigated participants. **a** First of two parts. **b** Second of two parts

Table 2 Relationship between χ and ϕ_m^q

χ	1	2	3	4
ϕ_m^q	π	0 and π	$0, 2\pi/3$, and $4\pi/3$	$0, \pi/2, \pi$, and $3\pi/2$

number of snapshots and demonstrates better performance than the INCM-volume approach.

To further analyze the reasons for the foregoing results, beam patterns of all the investigated approaches are generated, as shown in Fig. 9, where the average values from 200 Monte Carlo tests are illustrated. In Fig. 9b, the local enlargements for the interference locations are also demonstrated. Clearly, all the tested beamformers can accurately orient the mainlobe to the SOI. However, because the arbitrary gain and phase perturbation exists, all beamformers are unable to accurately form nulls at the DOAs of interferences, except for the optimal one. The gains of the GL-linear method to resist the two interferences are -42.17 dB and -45.49 dB, which are deeper than those of the INCM-ISV and INCM-linear methods but shallower than our proposed method and INCM-volume algorithm; thus, it presents a lower output curve than the latter two approaches in Fig. 8. The gains of the proposed algorithm for the two interferences are -50.26 dB and -55.38 dB, which are deeper than those of INCM-volume; therefore, our method attains the best output curve compared to several other methods.

4.5 Performance comparison of different interference intervals

In the last simulation, the effect of varying interference intervals on the output performance is tested and the mismatch model used in this part is analogous to the fourth scenario. Specifically, the θ_1 changes from 24° to 40° ; therefore, the gap between the two interferences varies from 16° to 0° . In other words, the region of the two interferences changes from separation to complete overlap. Moreover, the impact of χ on output SINR is also investigated. The relationship between χ and ϕ_m^q is listed in Table 2. The variations of output SINR against θ_1 with SNR = 20 dB and $K = 30$ are revealed in Fig. 10a. We see that the output curves of the GL-linear and INCM-linear methods show significant fluctuations with the change of θ_1 . The output curve for $\chi = 1$ is inferior to those of $\chi = 2, 3$, and 4, which are superior to other competitors. Figure 10b demonstrates the

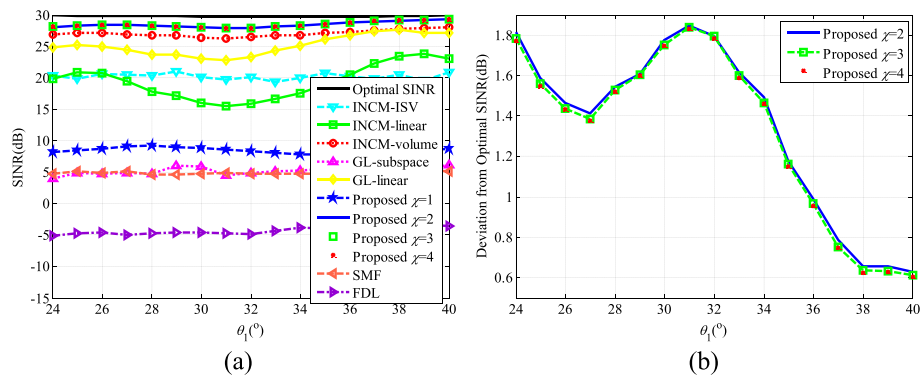


Fig. 10 Comparison of SINR for the last scenario. **a** SINR versus θ_1 . **b** Deviation from the optimal SINR against θ_1

plot of the deviation from optimal SINR versus θ_1 . It can be concluded that the performance for $\chi = 2, 3$, and 4 is almost converged to the same level, and the gaps between them are negligible. Overall, the use of $\chi = 2$ achieves a satisfactory output performance with the lowest computational cost.

5 Conclusions

In this study, a novel RAB algorithm on the basis of INCM reconstruction using the GLQ and SV estimation is proposed. The coefficients and nodes of the fifth-order GLQ are calculated, and a linear combination of the volume integral at five angular nodes is then computed to reconstruct the INCM. This procedure has reduced computational complexity. Based on several main eigenvectors of the SOI covariance matrix, the SV of SOI is obtained by a linear combination of these eigenvectors, and the double-constrained problem is converted to a single-constrained model, whose closed-form expression is yielded by the Lagrange multiplier method. The superior performance of our proposed algorithm is verified by several simulations including the comparisons for matrix correlation coefficients, running times, output SINRs yielded by different GLQ orders, DOA mismatches, gain and phase perturbation errors, as well as incoherent local scattering. Future work will concentrate on novel reconstruction methods of INCM to further reduce the computational complexity in terms of the integral within uncertainty sets.

Abbreviations

SOI	Signal of interest
INCM	Interference plus noise covariance matrix
GLQ	Gauss-Legendre quadrature
SV	Steering vector
SINR	Signal to interference plus noise ratio
DOA	Directions of arrival
RAB	Robust adaptive beamforming
SCM	Sample covariance matrix
SNR	Signal to noise ratio
SCB	Standard Capon beamformer
ULA	Uniform linear array
SMF	Spatial matched filter
FDL	Fixed diagonal loading

Acknowledgements

The authors would like to thank Prof. Jian Yang for his helpful communications during the preparation and revision of this paper.

Author contributions

YL was involved in conceptualization, methodology, and writing. FC helped in supervision and software. FW, CH, and XF contributed to review. All authors read and approved the final manuscript.

Funding

The work has been supported partly by the National Natural Science Foundation of China (Grant Nos. 61903375, 62071481, and 61773389), Natural Science Foundation of Shaanxi Province (2021KJXX-22, 2020JQ-298), Postdoctoral Science Foundation of China (2019M663635), and Special Support Plan for High-level Talents in Shaanxi Province (TZ0328).

Availability of data and materials

All data generated during this study are included in this published article.

Declarations**Ethics approval and consent to participate**

Not applicable.

Consent for publication

Not applicable.

Competing interests

The authors declare that they have no competing interests.

Received: 13 September 2022 Accepted: 29 December 2022

Published online: 13 January 2023

References

1. Y. Wang, Y. Shui, X. Yang et al., Multi-target vital signs detection using frequency-modulated continuous wave radar. *EURASIP J. Adv. Signal Process.* **2021**(1), 1–19 (2021)
2. F. Zhou, Z. Li, J. Cheng et al., Robust AN-aided beamforming and power splitting design for secure MISO cognitive radio with SWIPT. *IEEE Trans. Wirel. Commun.* **16**(4), 2450–2464 (2017)
3. Y. Lv, F. Cao, C. He et al., Covariance matrix reconstruction via a subspace method and spatial spectral estimation for robust adaptive beamforming. *Wirel. Commun. Mobile Comput.* (2022). <https://doi.org/10.1155/2022/9152752>
4. G. Tian, R. Song, Cooperative beamforming for a double-IRS-assisted wireless communication system. *EURASIP J. Adv. Signal Process.* **2021**(67), 1–10 (2021)
5. J. Xu, G. Liao, L. Huang et al., Robust adaptive beamforming for fast-moving target detection with FDA-STAP radar. *IEEE Trans. Signal Process.* **65**(4), 973–984 (2017)
6. B. Yang, W. Li, Y. Li et al., Robust adaptive beamforming based on automatic variable loading in array antenna. *Appl. Comput. Electromagn. Soc. J.* **36**(7), 908–913 (2021)
7. X. Zhang, Z. He, B. Liao et al., Robust quasi-adaptive beamforming against direction-of-arrival mismatch. *IEEE Trans. Aerosp. Electron. Syst.* **54**(3), 1197–1207 (2018)
8. M. Zhang, A. Zhang, Q. Yang, Robust adaptive beamforming based on conjugate gradient algorithms. *IEEE Trans. Signal Process.* **64**(22), 6046–6057 (2016)
9. J. Li, P. Stoica, Z. Wang, Doubly constrained robust Capon beamformer. *IEEE Trans. Signal Process.* **52**(9), 2407–2423 (2005)
10. Y. Huang, M. Zhou, S.A. Vorobyov, New designs on MVDR robust adaptive beamforming based on optimal steering vector estimation. *IEEE Trans. Signal Process.* **67**(14), 3624–3638 (2019)
11. S.A. Vorobyov, A.B. Gershman, Z. Luo, Robust adaptive beamforming using worst-case performance optimization: a solution to the signal mismatch problem. *IEEE Trans. Signal Process.* **51**(2), 313–324 (2003)
12. J. Qian, Z. He, J. Xie et al., Null broadening adaptive beamforming based on covariance matrix reconstruction and similarity constraint. *EURASIP J. Adv. Signal Process.* **2017**(1), 1–10 (2017)
13. Y. Ke, C. Zheng, R. Peng et al., Robust adaptive beamforming using noise reduction preprocessing-based fully automatic diagonal and steering vector estimation. *IEEE Access* **5**, 12974–12987 (2017)
14. Y. Gu, A. Leshem, Robust adaptive beamforming based on interference covariance matrix reconstruction and steering vector estimation. *IEEE Trans. Signal Process.* **60**(7), 3881–3885 (2012)
15. F. Chen, F. Shen, J. Song, Robust adaptive beamforming using low-complexity correlation coefficient calculation algorithms. *Electron. Lett.* **51**(6), 443–445 (2015)
16. Z. Zhang, W. Liu, W. Leng et al., Interference plus noise covariance matrix reconstruction via spatial power spectrum sampling for robust adaptive beamforming. *IEEE Signal Process. Lett.* **23**(1), 121–125 (2015)
17. S. Liu, X. Zhang, F. Yan et al., Fast and accurate covariance matrix reconstruction for adaptive beamforming using Gauss-Legendre quadrature. *J. Syst. Eng. Electron.* **32**(1), 38–43 (2021)
18. S. Mohammadzadeh, V.H. Nascimento, R.C. de Lamare et al., Maximum entropy-based interference-plus-noise covariance matrix reconstruction for robust adaptive beamforming. *IEEE Signal Process. Lett.* **27**, 845–849 (2020)
19. L. Huang, J. Zhang, X. Xu et al., Robust adaptive beamforming with a novel interference-plus-noise covariance matrix reconstruction method. *IEEE Trans. Signal Process.* **63**(7), 1643–1650 (2015)
20. X. Yang, Y. Li, F. Liu et al., Robust adaptive beamforming based on covariance matrix reconstruction with annular uncertainty set and vector space projection. *IEEE Antennas Wirel. Propag. Lett.* **20**(2), 130–134 (2020)
21. Z. Tan, W. Jia, W. Jin, Robust adaptive beamforming using k -means clustering: a solution to high complexity of the reconstruction-based algorithm. *Radioengineering* **27**(2), 595–601 (2018)

22. Z. Zheng, Y. Zheng, W. Wang et al., Covariance matrix reconstruction with interference steering vector and power estimation for robust adaptive beamforming. *IEEE Trans. Veh. Technol.* **67**(9), 8495–8503 (2018)
23. P. Chen, Y. Yang, Y. Wang et al., Adaptive beamforming with sensor position errors using covariance matrix construction based on subspace bases transition. *IEEE Signal Process. Lett.* **26**(1), 19–23 (2019)
24. H. Ruan, R.C. de Lamare, Robust adaptive beamforming based on low-rank and cross-correlation techniques. *IEEE Trans. Signal Process.* **64**(15), 3919–3932 (2016)
25. P. Zhang, Z. Yang, G. Jing et al., Adaptive beamforming via desired signal robust removal for interference-plus-noise covariance matrix reconstruction. *Circuits Syst. Signal Process.* **40**(1), 401–417 (2021)
26. X. Zhu, X. Xu, Z. Ye, Robust adaptive beamforming via subspace for interference covariance matrix reconstruction. *Signal Process.* **167**, 107289 (2020)
27. Y. Cheng, X. Zhang, M. Jin et al., Robust beamforming algorithm based on Gauss-Legendre integral. *J. Syst. Eng. Electron.* **43**(11), 3144–3150 (2021)
28. J. Gao, J. Zhen, Y. Lv et al., Beamforming technique based on adaptive diagonal loading in wireless access networks. *Ad Hoc Netw.* **107**, 102249 (2020)
29. J. He, T. Shu, V. Dakulagi et al., Simultaneous interference localization and array calibration for robust adaptive beamforming with partly calibrated arrays. *IEEE Trans. Aerosp. Electron. Syst.* **57**(5), 2850–2863 (2021)
30. X. Ke, Y. Zhao, L. Huang, On accurate source enumeration: a new Bayesian information criterion. *IEEE Trans. Signal Process.* **69**(1), 1012–1027 (2021)
31. X. Yuan, L. Gan, Robust adaptive beamforming via a novel subspace method for interference covariance matrix reconstruction. *Signal Process.* **130**, 233–242 (2017)
32. W. Zhang, J. Wang, S. Wu, Robust Capon beamforming against large DOA mismatch. *Signal Process.* **93**(4), 804–810 (2013)
33. F. Liu, R. Du, J. Wu et al., Multiple constrained ℓ_2 -norm minimization algorithm for adaptive beamforming. *IEEE Sens. J.* **18**(15), 6311–6318 (2018)

Publisher's Note

Springer Nature remains neutral with regard to jurisdictional claims in published maps and institutional affiliations.

Submit your manuscript to a SpringerOpen[®] journal and benefit from:

- Convenient online submission
- Rigorous peer review
- Open access: articles freely available online
- High visibility within the field
- Retaining the copyright to your article

Submit your next manuscript at ► [springeropen.com](https://www.springeropen.com)
